Materials Science and Engineering: A

COUNTRY	SUBJECT AREA AND CATEGORY	PUBLISHER	H-INDEX
Netherlands Universities and research institutions in Netherlands Media Ranking in Netherlands	Engineering Mechanical Engineering Mechanics of Materials Materials Science Materials Science (miscellaneous) Nanoscience and Nanotechnology Physics and Astronomy Condensed Matter Physics	Elsevier B.V.	277

PUBLICATION TYPE	ISSN	COVERAGE	INFORMATION
Journals	09215093	1988-2023	Homepage How to publish in this journal msea@elsevier.com

SCOPE

Materials Science and Engineering A provides an international medium for the publication of theoretical and experimental studies related to the load-bearing capacity of materials as influenced by their basic properties, processing history, microstructure and operating environment. Appropriate submissions to Materials Science and Engineering A should include scientific and/or engineering factors which affect the microstructure - strength relationships of materials and report the changes to mechanical behavior. Please be advised that the Aims and Scope for the journal has recently been updated. The journal will no longer consider or publish papers on concrete and cement-based systems nor on polymeric and polymer-based materials. In addition, papers with an emphasis on corrosion or wear are discouraged, unless they specifically address novel mechanical behavior or related phenomena.

Join the conversation about this journal

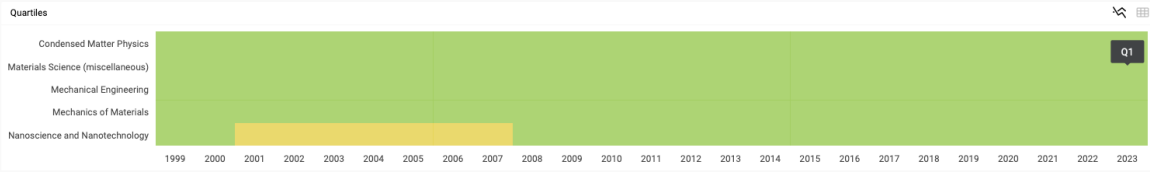

Materials Science & Engineering A 892 (2024) 146017

Contents lists available at ScienceDirect

Materials Science & Engineering A

journal homepage: www.elsevier.com/locate/msea

Improve the microstructure and properties of $Al_{0.5}CoCrFeNi$ compositionally complex alloy fabricated by selective laser melting with electropulsing treatment

Bo Jiao [a], Yuhui Du [a], Chunhuan Guo [a,*], Fengchun Jiang [a,b,**], Qianfei Sun [a], Hexin Zhang [a], Tao Dong [b], Zubin Chen [b], Sergey Konovalov [b,c]

[a] Key Laboratory of Superlight Materials & Surface Technology, Ministry of Education, College of Materials Science and Chemical Engineering, Harbin Engineering University, Harbin, 150001, China
[b] Yantai Research Institute and Graduate School of Harbin Engineering University, Yantai, 264006, China
[c] Siberian State Industrial University, 42 Kirov Street, Novokuznetsk, 654007, Russia

ARTICLE INFO

Keywords:
Electropulsing treatment
Selective laser melting
Compositionally complex alloy
Recrystallization
Mechanical properties

ABSTRACT

In order to improve the microstructure of the $Al_{0.5}CoCrFeNi$ compositionally complex alloy (CCA) prepared by selective laser melting (SLM), the electropulsing treatment (EPT) has been used as a post processing in this study. The strengthening and softening mechanism was analyzed by comparing the microstructure of SLM-$Al_{0.5}$CoCrFeNi CCAs under different EPT parameters. At a 10 s power on time, the substructure size of CCA decreases continuously with increasing voltage. Under 90V/10s EPT, the yield strength increases from 658 ± 10 MPa in the printed state to 748 ± 17 MPa, and the microhardness increases from 265.1 ± 5.6 $HV_{0.1}$ to 318.9 ± 5.0 $HV_{0.1}$. At 90V/20s EPT, the cellular substructure disappears, and a large number of uniformly distribute BCC phases precipitates inside the FCC matrix. At 90V/30s EPT, recrystallization occurs and the BCC phase coarsen. Dislocation network is the main factor that affects the strength of SLM-CCA. EPT can change the dislocation network structure to enhance the strength of SLM-CCA. Simultaneously, the EPT effectively promotes the transition from FCC phase to BCC phase in a short time. Joule heat and electronic wind force are the main reasons for changing structure and properties of SLM-$Al_{0.5}$CoCrFeNi CCA. This work provides a post-processing method named as EPT to effectively control the microstructure in additive manufacturing CCA products.

1. Introduction

High entropy alloy (HEA) is a new typical metal material with high mechanical strength, wear resistance, oxidation resistance and corrosion resistance discovered by Yeh and Cantor [1–6]. The HEAs contain 5 or more elements with the atomic fraction of each element between 5 % and 35 %, which are mainly composed of face-centered cubic (FCC), body-centered cubic (BCC), hexagonal close-packed (HCP) [4,7,8]. The subset of HEAs which contain multiple stable phases are referred to as compositionally complex alloys (CCAs) [9,10]. CCAs have obtained potential applications in aerospace, energy, biomedicine, marine and other fields [11].

Currently, the main synthesis routes of CCAs include arc melting, induction melting, and spark plasma sintering, while, it is difficult to produce CCAs components with complicated shapes [12–16]. In addition, coarse grain structure is easily formed in the casting process and the surface roughness is poor, which affects the product quality.

As an emerging technology, mental additive manufacturing (AM) has made significant breakthroughs in the shape, microstructure and efficiency compared with the traditional preparation methods of CCAs [4,17–20]. Selective laser melting (SLM) is a typical laser AM technology, which can selectively melts the metal powder on the powder bed layer by layer to form a solid metal structure [17]. It can use CCAs prealloyed powder to manufacture complex parts with high material utilization rate. The ultrafast cooling rate (about 10^5~10^6 °C/s) of SLM can refine the microstructure of CCA products and prevent the formation of

* Corresponding author.
** Corresponding author. Key Laboratory of Superlight Materials & Surface Technology, Ministry of Education, College of Materials Science and Chemical Engineering, Harbin Engineering University, Harbin, 150001, China.
E-mail addresses: guochunhuan@hrbeu.edu.cn (C. Guo), fengchunjiang@hrbeu.edu.cn (F. Jiang).

https://doi.org/10.1016/j.msea.2023.146017
Received 25 September 2023; Received in revised form 10 December 2023; Accepted 15 December 2023
Available online 24 December 2023

undesirable intermetallic compounds and the diffusion of constituent elements [21,22]. Due to the change in vacancy energy of the material before and after powder solidification, there are a large number of dislocations inside SLM-CCAs [23,24]. The high dislocation density in the printed sample results in high strength, which is very similar to the work hardening structure after deformation. However, extremely rapid melting and solidification of the molten pool during the process of SLM produce a large temperature gradient, which will generate a lot of shrinkage cavities, coarse columnar crystal structures and residual stress in the manufactured parts [25–28]. SLM-alloys often suffer from poor plasticity, and usually require further heat treatment or hot isostatic pressing treatment, in order to remove internal stress and regulate plasticity and strength [29]. Fujieda et al. carried out solution treatment (ST) on $Co_{1.5}CrFeNi_{1.5}Ti_{0.5}Mo_{0.1}$ HEA produced by selective electron beam melting (SEBM), the tensile properties and corrosion properties of the sample were significantly improved [30]. Joseph et al. found that hot isostatic pressing (HIP) can reduce the porosity and improve the mechanical properties of $Al_xCoCrFeNi$ CCAs deposited by direct laser deposition [31]. Cui et al. used ultrasonic surface rolling treatment (USRP) to roll the CrMnFeCoNi HEA prepared by laser additive manufacturing technology, and obtained a nanocrystalline layer on the surface of the HEA, with a hardness of 5.2 GPa [32]. However, it is difficult to apply ultrasonic rolling treatment to complex geometric components [33]. Traditional heat treatment technology takes a long time, wastes energy and easily causes coarse grains.

Recently, many investigations show electropulsing can decrease deformation resistance, reduce surface oxidation and decrease recrystallization temperature [34]. For example, Xu et al. successfully prepared Ti–6Al–4V alloy with high yield strength (1280 MPa), excellent strength (1358 MPa) and elongation (13.7 %) by using electropulsing treatment (EPT) [35]. Pan et al. improved the yield strength and elongation of AA6061 alloy samples by 72.1 % and 2.1 % respectively by cyclic EPT. The latest research attributed the principle of improving microstructure by EPT to the thermal effect caused by Joule heat and the athermal effect caused by electronic wind force [36–39]. Joule heat can induce the material to rise in temperature, leading to recovery and recrystallization [40]. As-cast alloys often store a large amount of energy through cold plastic deformation, resulting in severe lattice distortion of the grains as the driving force for recrystallization. The dislocation density of printed HEAs is about 10^{13} - $10^{15}/m^2$ [21,23]. This is similar to the work hardening structure after deformation, which is more likely to cause recrystallization under post-treatment. The typical theory explaining athermal effects is the electron wind theory [41,42]. The drift electrons can apply electron wind force to dislocations to improve the plasticity of metals, which is called the electroplastic effect [40,41,43]. The reduction of material flow stress is believed to be directly attributed to the momentum transfer from the electric field, which assists in the movement of dislocations within the metal lattice [44]. The interaction of moving electrons in a metal crystal with the dislocations therein was first reported by Troitskii in 1963 [45]. Tang et al. found that current pulses reduced the force required for drawing and rolling, and significantly improved the plasticity of the deformation zone [46,47]. Zhang et al. directly proved that electron force can promote dislocation movement by comparing electric in-situ TEM with heating in-situ TEM experiments [41]. These results indicate that electronic wind has a significant impact on the flow stress of metals. However, there is limited research on the effects of EPT on the microstructure and properties of SLM-CCAs.

Based on the above mentioned, in order to improve the microstructure of $Al_{0.5}CoCrFeNi$ CCA fabricated by SLM, the EPT has been proposed. And the effect of EPT on the microstructure and mechanical properties of the SLM-$Al_{0.5}CoCrFeNi$ CCA has been analyzed. The strengthening and softening mechanisms of SLM-CCAs under different EPT parameters have been fully revealed. This work brings forward an effective strategy to rapidly design a high-performance SLM-CCA based on the change of the dislocation network and recrystallization.

2. Materials and experiments

2.1. Material and SLM process

The high purity gas atomized $Al_{0.5}CoCrFeNi$ CCA powder with an average particle diameter of 15–53 μm was used in this study. The samples were fabricated by an AFS-M260 SLM system (Longyuan AFS Co., Ltd, China) with maximum 500 W fiber laser power output and typically 70 μm diameter laser spot. The SLM process was carried out in an argon-proctected atmosphere. The substrate is made of a 260 × 260 × 25 mm^3 316 stainless steel. To reduce the cooling rate, the substrate is preheated to 100 °C before printing. The optimized parameters with laser power 200 W, scanning speed 0.8 m/s, layer thickness 40 μm, scanning interval 90 μm, and laser rotation 67° between each layer. A 70 × 10 × 3.5 mm^3 sample is constructed by repeating this process.

2.2. EPT process

The SLMed bulks were cut into platelike samples with 70 × 10 × 1.8 mm^3 using wire electrical discharging machine, and the thickness direction is along the building direction (Fig. 1b). The CCA samples are polished with 3000-grit SiC paper to maintain sufficient electrical contact, and then clamp it with two copper electrodes. As illustrated in Fig. 1a, the EPT experiments were carried out at room temperature by a THDM-II electropulsing generator, and the rated power is 30 kW, the maximum output voltage is 150 V, the maximum peak current is 5000 A, the operating frequency is in a range of 100–800 Hz. The CCA samples were electropulsing treated from 30 V to 90 V followed by air cooling, the specific process parameters are shown in Table 1. To assess the Joule heat during the EPT, the temperature of the CCAs were measured by an infrared thermal imager (Fig. S1). The CCA samples processed under different parameters are shown in Fig. 1c.

2.3. Characterization

Phase detection was performed on a X-ray diffraction (XRD) equipment with Cu-Kα radiation, scanning angles ranging from 30° to 90° and a scanning speed of 4°/min. Optical microscopy (OM), Scanning Electron Microscope (SEM) and Electron Backscatter Diffraction (EBSD) were used to characterize the microstructure of samples. The samples for OM observations were polished and chemically etched inetching solution of 10 % nitric acid, 30 % hydrochloric acid and 60 % distilled water. SEM and EBSD measurements were carried out on a JEOL JSM-7900F SEM. The acceleration voltage is 15 kV, the working distance is about 14.5 mm, and the step size is 2 μm. EBSD specimens were mechanically polished and then ion-beam polished. AZtecCrystal software was used to analyze the grain morphology, textures, kernel average misorientation and dislocation density of the SLMed and 90V/30s state. The tensile test was performed with a loading rate of 0.5 mm/min at room temperature, and dimensions of the flat dog bone shaped tensile specimen is shown in the inset image of Fig. 7a. At least three tests were performed for the same condition to ensure reproducibility of the results. The yield strength was determined using the 0.2 % offset plastic strain method. The HVS-1000A microhardness tester was used to test the microhardness of SLM-CCAs with and without EPT, with the load of 1000 g and the loading time of 10s. At least ten indentations were measured for each point to obtain an average value. Randomly select 100 subgrains from two SEM images of each sample for size measurement and frequency distribution statistics.

3. Results

3.1. Microstructure

The optical micrographs of the SLM-$Al_{0.5}CoCrFeNi$ samples with different EPT states are shown in Fig. 2. It can be seen that the CCAs

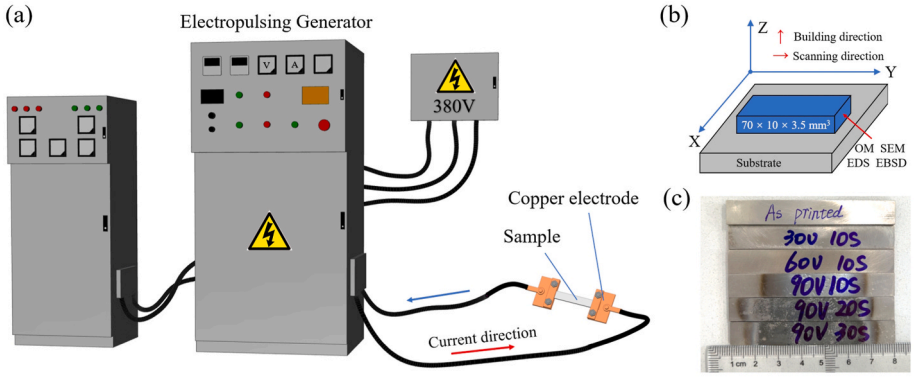

Fig. 1. (a) Schematic diagram of EPT. (b) Configuration and orientation of SLM and characterization specimens. (c) Image of the samples with different EPT states.

Table 1
Processing parameters of EPT for the SLM-$Al_{0.5}$CoCrFeNi CCAs.

Sample code	Frequency (Hz)	EPT Voltages (V)	Processing time (s)	Temperature (°C)
SLMed	–	–	–	–
30V/10s	350	30	10	64.1
60V/10s	350	60	10	223.0
90V/10s	350	90	10	352.8
90V/20s	350	90	20	530.5
90V/30s	350	90	30	713.1

exhibit a clear fish scale like molten pool morphology, and the epitaxial columnar grains grow along the building direction. Clearly, the epitaxial columnar grains grow under the temperature gradient during the SLM process, which is consistent with the previous reports elsewhere [4]. The short EPT time cannot alter such crystal structure, however, the internal columnar crystal diameter of the CCA increases with increasing EPT voltage under the 10 s processing time. As shown in Fig. 2a, the grain size in the printed state is the smallest, with maximum and minimum widths of 113.2 μm and 68.8 μm, respectively. When the EPT voltage rises to 90 V, the columnar crystal size inside the CCA is the largest, and the maximum width can reach 201.5 μm (Fig. 2d). The increased voltage brings higher Joule heat, while the number of drift electrons inside the metal increases. The effects of Joule heating and electron wind force promote the movement of metal atoms inside high entropy alloys, increase the size of columnar grains [36,39]. When processing at 90 V voltage for more than 20 s, the boundary of the molten pool disappears and a large amount of precipitates appear. After the EPT time reaches 30 s, an equiaxed crystal structure is formed, and the size of the precipitate phase significantly increases.

The XRD results of the SLM-$Al_{0.5}$CoCrFeNi CCA samples with and without EPT are shown in Fig. 3. The patterns revealed that the 90V/20s and 90V/30s samples consisted of the major FCC phase and a minor (110) reflection of the BCC phase and other samples exhibit a single-phase FCC microstructure. This is consistent with the phase composition of $Al_{0.5}$CoCrFeNi CCAs obtained by traditional heat treatment process, the FCC phase transforms to BCC phase during EPT [48]. Previous studies have interpreted it as that the Al–Ni rich phase have a higher negative mixing enthalpy than the other atom pairs of the five main elements in the alloy system [49]. It can also be seen from the XRD that the peak intensity of BCC phase reaches the maximum in 90V/20s sample.

Fig. 4 shows SEM images under different EPT conditions. Similar to other SLM-CCAs, massive columnar and cellular substructures exist inside each columnar grain [23]. Its shape varies depending on the sampling direction. Related researchers have found a large number of dislocations at the boundary of the substructure, known as the “dislocation network” [50]. The diameters of these subgrains will have a significant impact on the tensile mechanical properties of SLM-$Al_{0.5}$CoCrFeNi, which is discussed in detail in section 4.1. Fig. 4e shows dislocation cell network disappear after 90V/20s EPT. A large amount of elliptical and needle shaped precipitates appear inside the grains. A small amount of precipitates are interconnected to form bands similar to grain boundaries. After 90V/30s treatment, the precipitation phase at

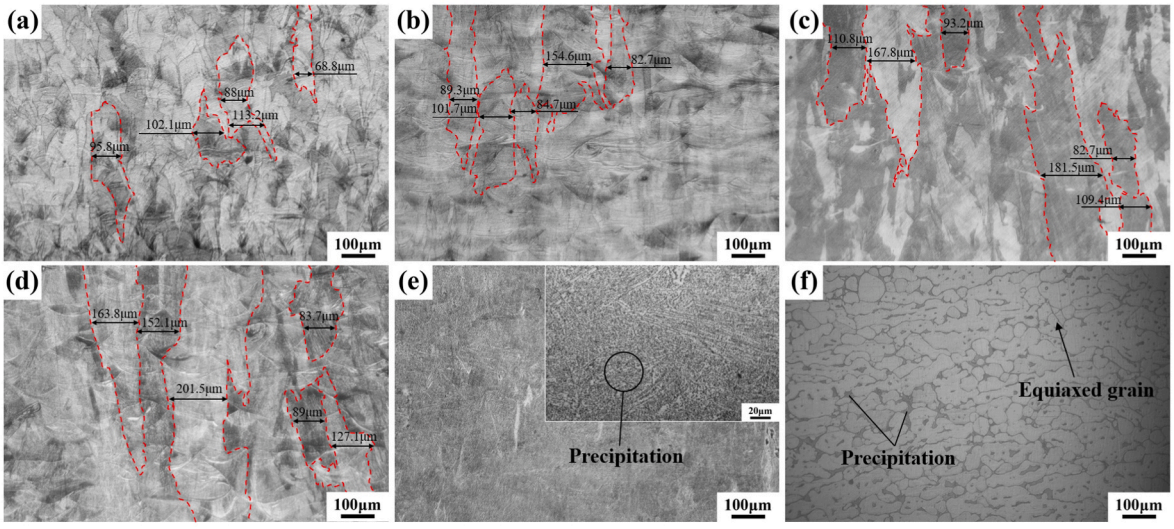

Fig. 2. OM images of (a) SLM-$Al_{0.5}$CoCrFeNi CCA; (b) 30V/10s EPT; (c) 60V/10s EPT; (d) 90V/10s EPT; (e) 90V/20s EPT; (f) 90V/30s EPT.

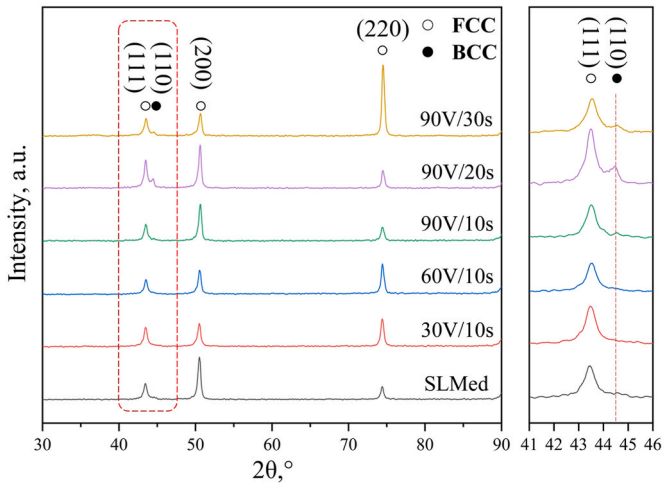

Fig. 3. The XRD of SLM-$Al_{0.5}$CoCrFeNi CCA with and without EPT.

the grain boundary preferentially nucleates and grows, while the recrystallized structure is completely formed, as shown in Fig. 4f. The partitioning of elements into these phases in 90V/20s EPT was determined by SEM-EDS, shown in Fig. 5a. It is obvious that the BCC phase rich in Al and Ni is dispersed in the FCC matrix. In the 90V/30s state, the BCC phase rich in Al and Ni coarsens at the boundary of FCC grains (Fig. 5b). Obviously, the temperature rise causes the SLM-$Al_{0.5}$FeCoCrNi recovery and recrystallization due to Joule heat.

To further identify the microstructural evolution of SLM-$Al_{0.5}$CoCrFeNi CCA before and after recrystallization created by the EPT. The samples with 90V/30s EPT and without EPT are analyzed using EBSD, as shown in Fig. 6. As can be seen from the inverse pole figures (Fig. 6a and b), the original epitaxial columnar grains have completely disappeared, replaced by randomly oriented recrystallized grains after 90V/30s EPT. Furthermore, phase identification for FCC and BCC phases are determined by EBSD date, as shown in Fig. 6c and d. Due to the repeated thermal cycles experienced by the CCA during the SLM process, a small amount of BCC phases are precipitated in situ during the thermal cycling process of the printed high entropy alloy, and the proportion of BCC phase precipitated in situ is 0.21 %. As shown in Fig. 6d, the precipitation content of BCC increases from 0.21 % in the printed state to 5.3 % after 90V/30s EPT, mainly precipitated at grain boundaries. This is consistent with the phase composition analysis results of XRD.

To investigate the effect of EPT on the microstructure of SLM-$Al_{0.5}$CoCrFeNi, microstructure analysis was conducted on the selected area of EBSD. To assess the changes in crystallographic texture by EPT, the IPF for the {001}, {101}, and {111} crystal plane families are constructed using the EBSD data. As shown in Fig. 6e and f, the SLM-$Al_{0.5}$CoCrFeNi CCA exhibits a clear crystallographic orientation in the <001>//X direction, with a maximum texture strength of 4.89. The maximum texture strength decreases to 3.69 after 90V/30s EPT. The EPT causes recrystallization to weaken the formation of <001> directional textures in the printed CCA, while no other directional textures are observed. These experimental results further indicate that EPT can promote the SLM-$Al_{0.5}$CoCrFeNi to form recrystallization in a very short period of time, thereby changing the anisotropic mechanical properties of printed parts.

3.2. Mechanical properties

Fig. 7a shows the tensile engineering stress-strain curves of SLM-$Al_{0.5}$CoCrFeNi CCAs with different parameters EPT and without EPT. It can be seen that within the same processing time of 10 s, the strength continuously increases with increasing of voltage. The maximum value is reached after 90V/10s EPT, with a yield strength of 748 ± 17 MPa, a tensile strength of 982 ± 12 MPa, and an elongation of 21.9 %. Compared with the SLM-CCA, the yield strength increases by about 13.7 % (from 658 ± 10 MPa to 748 ± 17 MPa), and the elongation slightly increases (from 20.1 % to 21.9 %). As shown in Fig. 7b, it is found that the SLM-$Al_{0.5}$CoCrFeNi CCA reprocessed by 90V/10s EPT shows significant improvement in strength and ductility compared to different manufactured $Al_{0.5}$CoCrFeNi CCAs treated by other post treatment methods [4,51–56]. From the comparison, 90V/10s EPT sample exhibits relatively high yield strength while maintaining considerable elongation. At a voltage of 90V, as the EPT time increases, the material continues to soften and its strength gradually decreases. Under the EPT of 90V/20s and 90V/30s, the yield strengthes of the CCAs are 513 ± 6 MPa and 425 ± 9 MPa, and the elongations are 28.9 % and 35 %, respectively. Interestingly, the yield strength increases slightly while the elongation increases by 20 % after 30V/10s EPT.

Fig. 8 shows the microhardness of the SLM-$Al_{0.5}$CoCrFeNi CCAs with and without EPT. It can be seen that the trend of change in microhardness is the same as that of yield strength. At a power on time of 10 s, the average microhardness of CCA increased by ~20.4 % (from 265.1 ± 5.6 $HV_{0.1}$ to 318.9 ± 5.0 $HV_{0.1}$) as the voltage increases. Under the conditions of 90V/20s and 90V/30s, the microhardness decreases to 289.2 ± 2.5 $HV_{0.1}$ and 208.9 ± 5.0 $HV_{0.1}$, respectively. Obviously, EPT

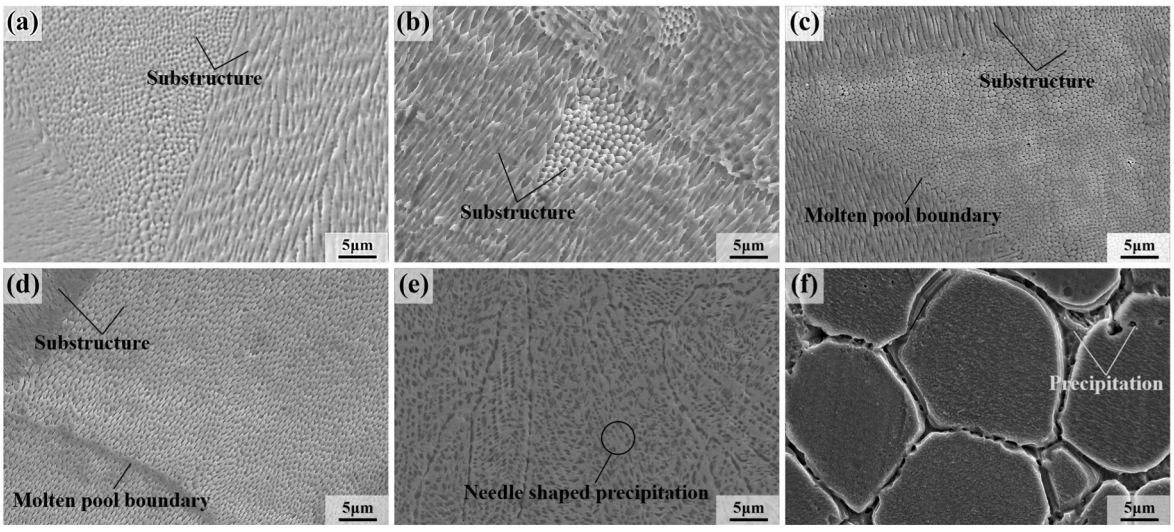

Fig. 4. SEM images of (a) SLM-$Al_{0.5}$CoCrFeNi CCA; (b) 30V/10s EPT; (c) 60V/10s EPT; (d) 90V/10s EPT; (e) 90V/20s EPT; (f) 90V/30s EPT.

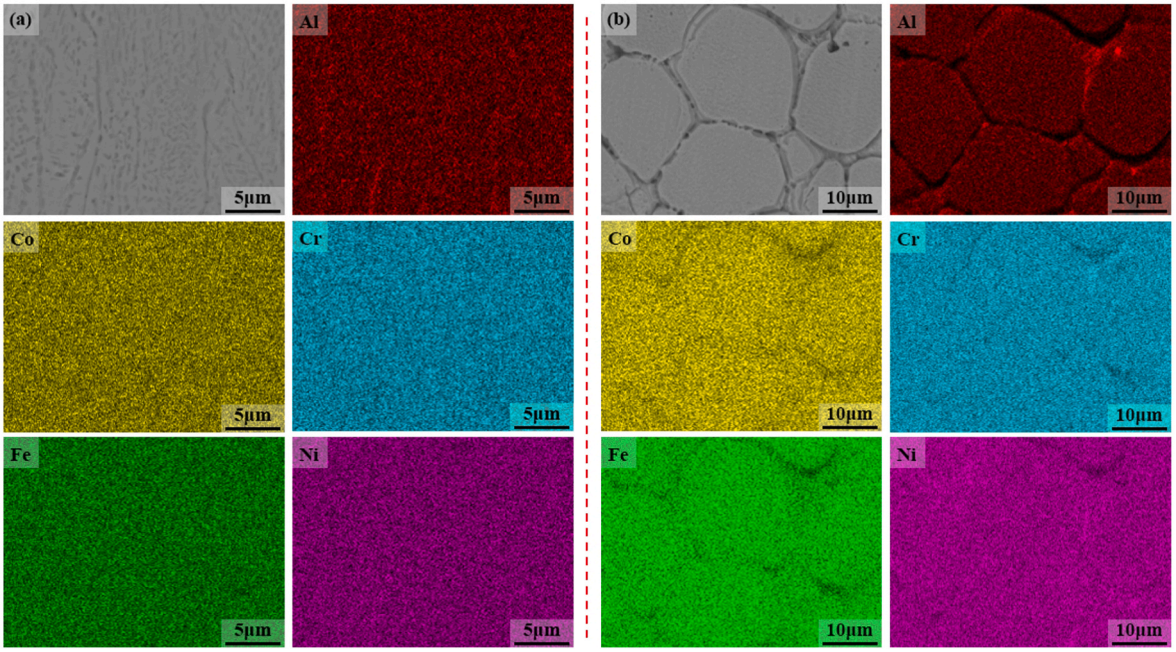

Fig. 5. Qualitative elemental distribution EDS maps of the EPT sample. (a) 90V/20s EPT sample. (b) 90V/30s EPT sample.

can achieve ideal performance of SLM-CCAs in a short period of time by adjusting processing parameters.

Fig. 9 shows the tensile fracture surface characteristics of SLM-$Al_{0.5}$CoCrFeNi with and without EPT. Typical dimple characteristics are observed in all samples, indicating that all alloys have undergone considerable plastic deformation and failed in ductile fracture mode. A large number of elongated dimples are observed in Fig. 9b. The dimples in SLMed state of Fig. 9a are small, and their number density is the largest. Compared with the SLMed state, the dimples of 30V/10s, 60V/10a and 90V/10s are larger and deeper, indicating that EPT slightly improves the plasticity of the CCA. This is consistent with the results of the tensile stress-strain curve. Under 90V/20s and 90V/30s EPT, the fracture surface is mainly composed of cleavage facets (area A) and tearing ridge and some large size ductile dimples in Fig. 9e and f. The fracture mode is a mixture of quasi-cleavage and ductile fracture. As is well known, the size and quantity of the second phase determine the size and quantity of dimples. Therefore, it can be concluded that the second phase of this specimen is greater than that of other specimens, which is consistent with SEM results. When sufficient stress is applied to break the interface bond between the particles and the matrix, voids will form around the second phase particles, leading to final fracture. However, extra large dimples are observed in samples treated at higher energy and two samples exhibit good plasticity.

4. Discussion

4.1. Strengthening and softening mechanism

Massive subgrains exist in SLM-$Al_{0.5}$CoCrFeNi, which is a unique structure in additive manufacturing technology (Fig. 4a). In our previous research [57], it has been fully confirmed that the dislocation network within CCA divides grains into many small substructures. This phenomenon is caused by the difference in vacancy energy between solids and liquids. In the liquid melt pool, vacancy energy is low and vacancies are abundant. When in solid state, the vacancy energy is high. During the solidification process of traditional preparation methods, vacancies are gradually filled up. However, the rapid solidification process in additive manufacturing and the slow diffusion in CCAs hinder the filling of vacancies. Therefore, many vacancies are retained in the printed material, which in turn merge into a large number of dislocations [50,58]. The dislocation network is one of the major strengthening mechanisms of SLM-CCA, which maintains lattice continuity and hinders the movement of dislocations during deformation. This can be clearly seen from the kernel average misorientation (KAM) distribution map of the sample by EBSD date, as shown in Fig. 6i. The mutual constraints between columnar grains in the molten pool during solidification process promote a high KAM values inside the SLM-CCA. In our recent work, the characteristics of the SLM-$Al_{0.5}$CoCrFeNi dislocation network have been fully studied through TEM [57]. There are a large number of dislocations inside SLM-CCA, which can be used as a reference to estimate dislocation density through KAM. The dislocation density value at the grain boundary within the region can be calculated according to the following equation.

$$\rho^{GND} = \frac{2KAM_{ave}}{\mu b} \tag{1}$$

In formula (1), ρ^{GND} is the density of geometrically necessary dislocations (GND), KAM_{ave} is the average value of KAM, μ is the step size used in EBSD testing, and b is the length of the Bernoulli vector. The average KAM of the SLM-$Al_{0.5}$CoCrFeNi is 0.77°, and the average dislocation density is 0.84×10^{14} m^{-2}. Fig. S2 shows the GNDs distribution of the SLMed and 90V/30s samples.

Notably, EPT can promote the movement of dislocations within CCA. Under the action of pulse current, dislocations within the CCA undergo annihilation and rearrangement. This change can be reflected in the different sizes of cellular substructures. Fig. 10a is a schematic diagram of the diameter distribution of subgrains with printed and different EPT states under 10s process time. The size range of SLM-$Al_{0.5}$CoCrFeNi subgrains is the largest, with an average diameter of 0.734 μm. After a 30V/10s EPT, the average diameter of the subgrains is 0.691 μm. Among them, the proportion of substructure sizes in the range of 0.6–0.7 μm is the highest, accounting for 39 %. When the EPT voltage is 60 V, the average diameter of the CCA substructure is 0.668 μm. The substructure at 0.4–0.5 μm disappears, and the proportion of substructure at 0.6–0.8 μm significantly increases. After 90V/10s EPT, the average diameter of the CCA subgrain is 0.558 μm. The subgrains with a size greater than 0.9 μm disappears and a substructure with a size less than 0.4 μm appears. Obviously, In a shorter EPT time, the size of the SLM-$Al_{0.5}$CoCrFeNi

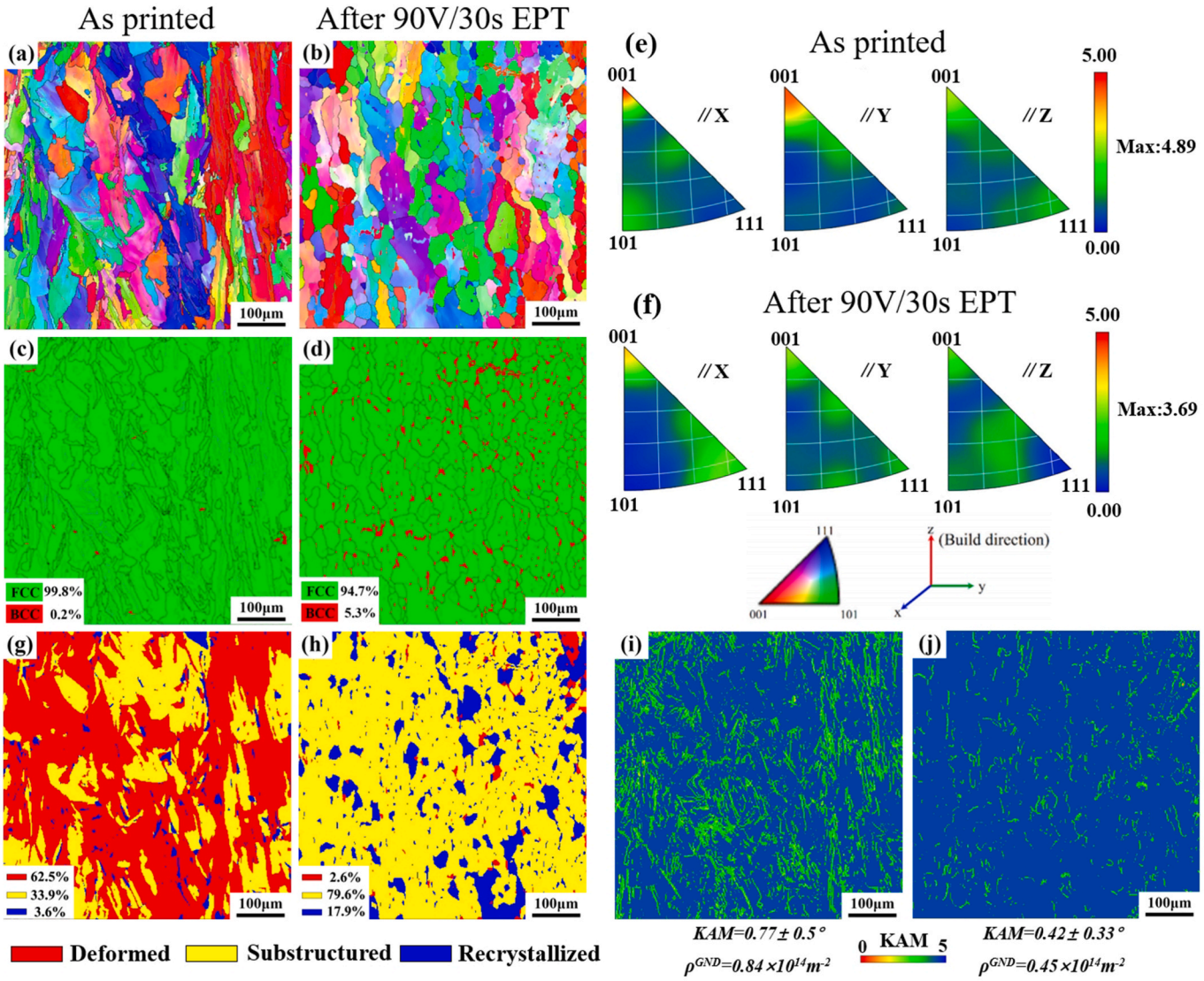

Fig. 6. Inverse pole figures of (a) SLM-$Al_{0.5}$CoCrFeNi CCA (b) 90V/30s EPT state. Phase identification for FCC and BCC phases in samples with (c) SLM-$Al_{0.5}$CoCrFeNi CCA (d) 90V/30s EPT state. IPF for (e) SLM-$Al_{0.5}$CoCrFeNi CCA (f) 90V/30s EPT state. Recrystallization distribution maps of (g) SLM-$Al_{0.5}$CoCrFeNi CCA (h) 90V/30s EPT state. KAM maps of (i) SLM-$Al_{0.5}$CoCrFeNi CCA (j) 90V/30s EPT state.

substructure decreases with increasing voltage. The tensile test results show that under 10s EPT time, the yield strength increases with increasing voltage. It reaches 672 ± 12 MPa and 681 ± 14 MPa under 30V/10s and 60V/10s EPT, respectively. And up to the highest 748 ± 17 MPa under 90V/10s EPT, which is about 13.7 % higher than the printed state. The yield strength of CCAs is usually determined by four strengthening mechanisms, including grain boundary strengthening, dislocation strengthening, solid solution strengthening, and precipitation strengthening [59]. In fact, several samples processed in 10s show a single FCC phase formation, and the grain size gradually increases under the action of Joule heating. Obviously, dislocation strengthening is the main reason for the increase in strength. It can be seen that the dislocation structure rearranged under EPT, which is the main factor affecting the mechanical properties of CCA. The reduction of dislocation density and rearrangement of dislocation structures under the action of electric pulses have been widely reported [60,61]. Xiang et al. found that electron wind force can lead to a decrease in the dislocation multiplication rate of Frank Read source under the action of high current density [39]. The final dislocation density decreases and the dislocations are generally arranged in parallel. However, in this study, it is found that dislocations exhibit a close packing before parallel arrangement under the action of lower current density.

A classic Frank-Read source models introduced in previous studies can be employed to explain this point [39]. The electron wind force applied to dislocation AB that is aligned with the drift electron direction. As shown in Fig. 10b, when point A is pinned, dislocations develop from line 0 to 4 under the different levels of electron wind forces. Finally, dislocations parallel to the direction of drift electrons, like line 4, move forward to the grain boundary or annihilate. When point A and B are both pinned, dislocations form arcs such as line 0 to 3 under the different levels of electron wind forces. Fig. 10c shows the actual dislocation structures predicted by Fig. 10b, corresponding to the samples in this study.

Theoretical considerations of the force exerted by drift electrons on dislocations were given by Klimov et al. [42].

$$\frac{f_{ed}}{l} = \frac{1}{3} nm^* b v_F (v_e - v_d) = \frac{m^* b V_F}{3e} J \tag{2}$$

where $\frac{f_{ed}}{l}$ is the force per unit length acting on the dislocation, v_e is the electron velocity, b is the Burgers vector, e is the electron charge, J is the current density, n is the electron density, m^* is the effective electron mass, v_F is the Fermi velocity, v_d is the dislocation velocity.

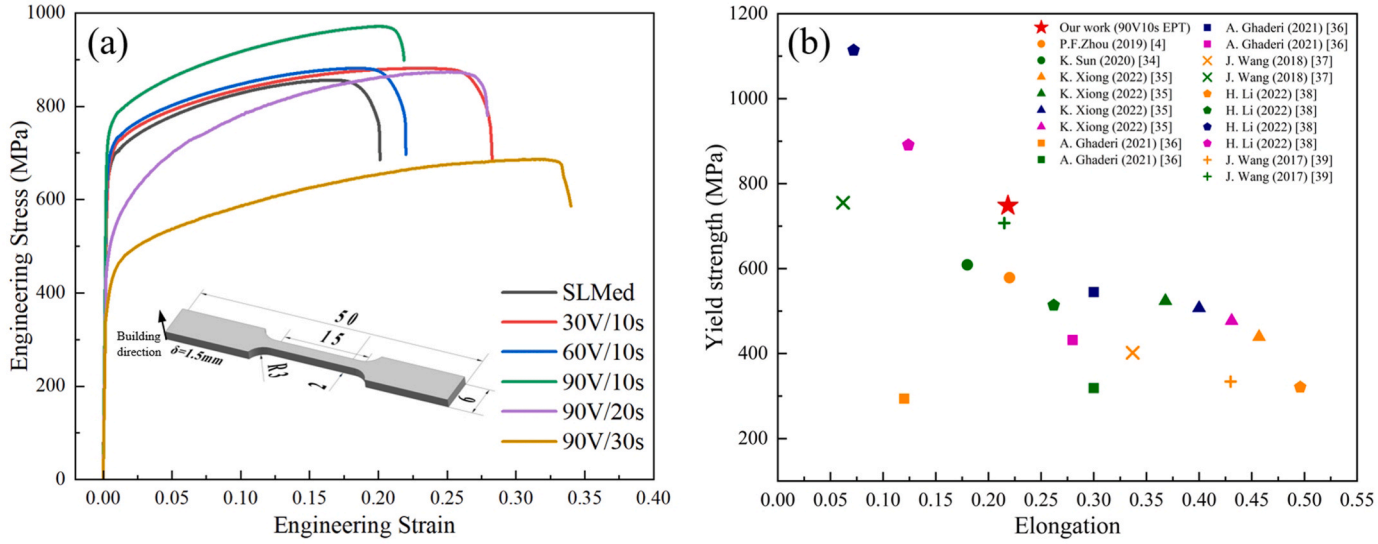

Fig. 7. (a) Tensile engineering stress-strain curves of the SLM-$Al_{0.5}$CoCrFeNi CCAs with and without EPT. (b) Yield strength and ductility data of SLM-$Al_{0.5}$CoCrFeNi CCA reprocessed by EPT and $Al_{0.5}$CoCrFeNi CCAs prepared by other methods.

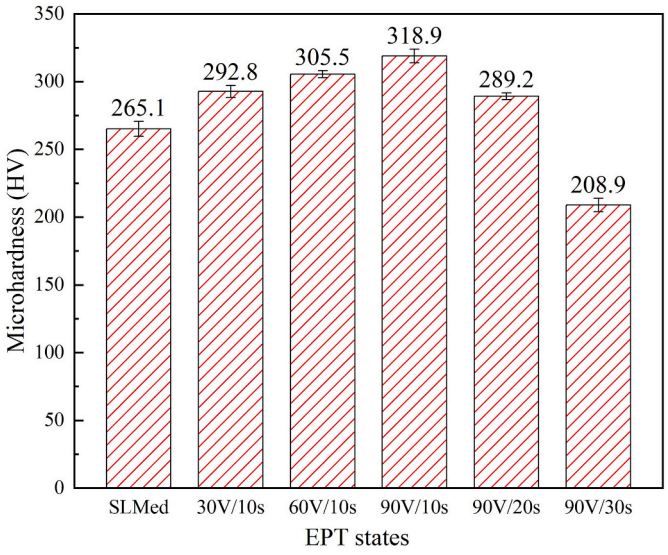

Fig. 8. Average microhardness of the SLM-CCAs with and without EPT.

In this consideration, the force due to the drift electrons is proportional to the drift electron velocity v_e (assuming that the dislocation is temporarily held up at some obstacle, $v_d = 0$). Further, the drift electron velocity v_e is proportional to the current density, namely, the electron wind force $\frac{f_{ed}}{l}$ is proportional to the current density. Therefore, the electronic wind force increases with increasing electrified voltage. Under the action of electronic wind force, the original dislocation network forms different levels of distortion. In the dislocation distortion zone, some atoms leave their original equilibrium positions, resulting in a stress field that increases the interaction between the dislocation network and the moving dislocation, increasing the slip resistance of the dislocation and thereby improving the strength of the material. The substructure exhibits a finer morphology after dislocation network squeezed by electronic wind force. At a processing time of 10 s, although the grain size continuously increases under the Joule heating effect, the yield strength continuously increases with increasing voltage. It can be seen that changes in dislocation structure can strengthen SLM-$Al_{0.5}$CoCrFeNi CCA under lower energy level electrical pulse processing.

In addition, the microhardness results indicate that the hardness value of 90V/10s is the highest, which is also beneficial by the refinement of the substructure. However, the continuous increased EPT time accumulated more Joule heat, resulting in a decrease in dislocation density and softening of the sample.

At 90V/20s and 90V/30s EPT states, the yield strengths of CCAs has significantly decreased to 513 ± 6 MPa and 425 ± 9 MPa, respectively. Typically, temperature rise cause vacancies to be filled or relocate, thereby reducing dislocation density. However, the precipitation of hard BCC phase and the continuous decomposition of dislocation network can both alter the mechanical properties of the sample. The boundary of the dislocation network can serve as the nucleation site for precipitates, preferentially forming BCC phase. Under 90V/20s EPT, a large number of precipitates are formed at the boundary of the dislocation network. In previous studies [57], uniformly distributed hard and brittle precipitates can hinder the movement of dislocations and significantly improve the strength of CCA. Compared with SLMed CCA, the yield strength of CCA under 90V/20s EPT decreased by 22.0 %, and the elongation after fracture increased by 43.8 %. It can be seen that the continuous decomposition of dislocation networks is the main reason for changing the mechanical properties of the sample. At 90V/30s EPT, the microstructure is completely composed of recrystallized grains. As shown in Fig. 6j, the dislocation density in the recrystallized structure is only 53.6 % of the printed state.

Let's summarize the changes in microstructure during the recrystallization. In the early stages of EPT processing, electronic wind force dominates. Under the action of directional electronic wind force, the dislocation network is pulled and deformed. And the dislocation network pile-up and forms a dislocation wall. With the EPT processing time increases, Joule heat accumulates to a certain extent, replacing electronic wind power as the dominant force. The melting point of the dislocation wall is relatively low, and the decomposition of dislocations occurs first. The electronic wind force promotes the deflection and motion of the dislocation network boundary, which also accelerates its annihilation. Meanwhile, the BCC phase prioritize the precipitation of dislocation network positions. Finally, the dislocation network is completely decomposed, and the BCC phase aggregates and forms a recrystallized structure. The strengthening of dislocations in the recrystallized grains is significantly weakened, and the strengthening of dislocation networks is eliminated.

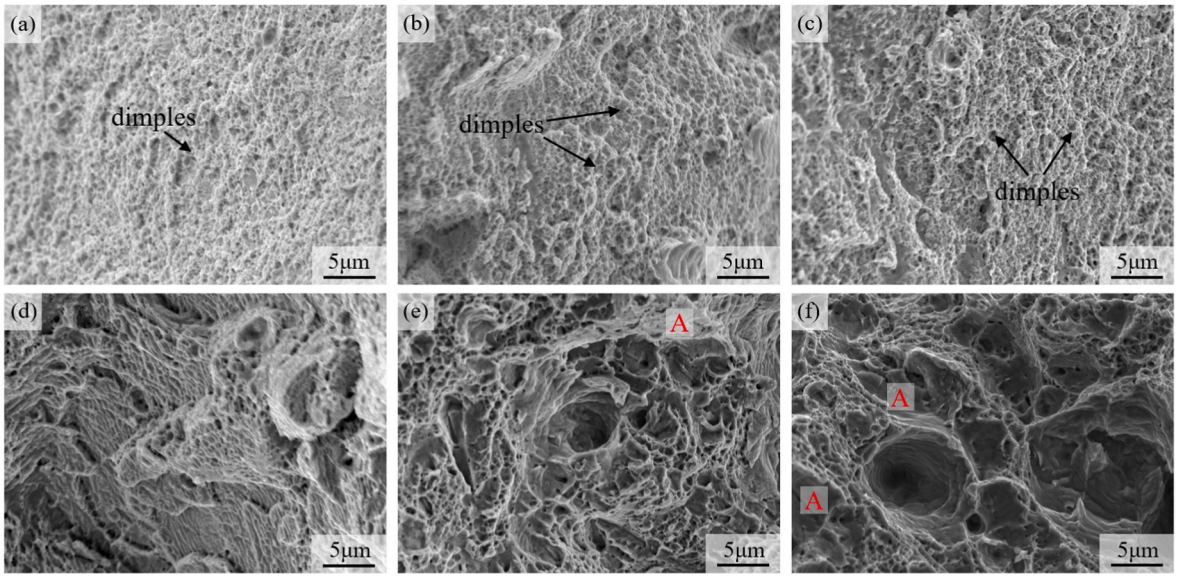

Fig. 9. Fracture surface of (a) SLMed, (b) 30V/10s, (c) 60V/10s, (d) 90V/10s, (e) 90V/20s, (f) 90V/30s.

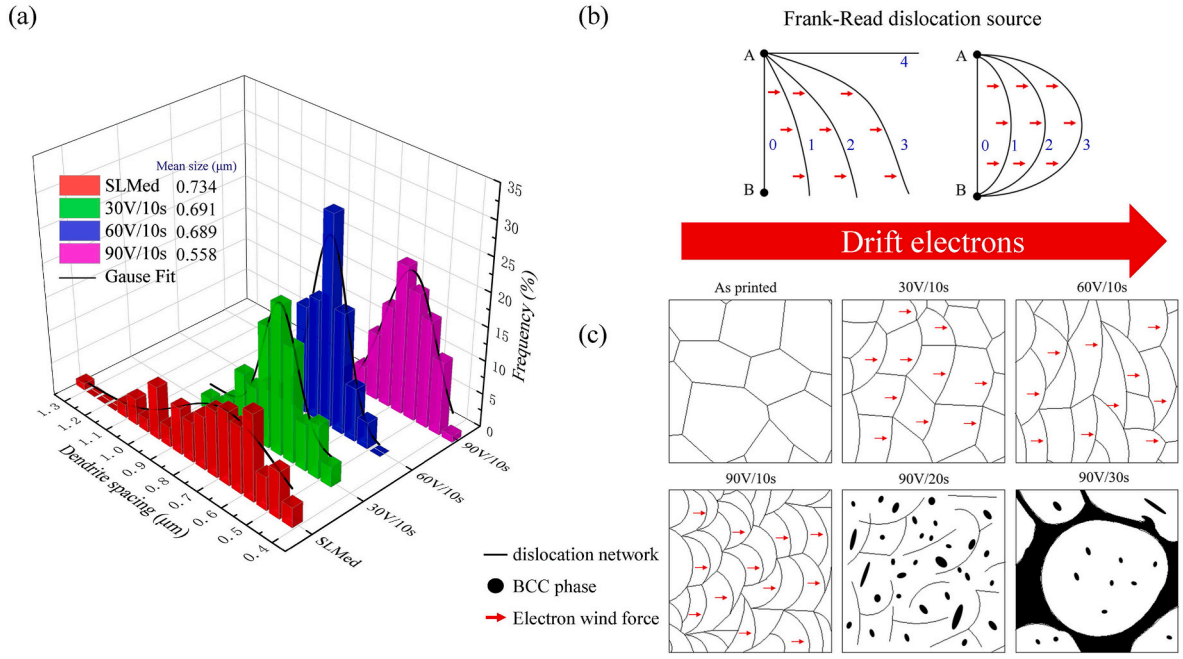

Fig. 10. (a) Statistical diagram of subgrain diameter of SLMed, 30V/10s, 60V/10s and 90V/10s states. (b) Schematic diagram of deformation prediction of Frank Read source under the action of electronic wind force. (c) Schematic diagram for substructure evolution of SLM-$Al_{0.5}$CoCrFeNi CCA at different EPT conditions.

4.2. Recrystallization

Compared with the single thermal effect mechanism of traditional heat treatment, EPT has a unique synchronous effect of thermal and non thermal effects. Instantaneous high-energy input can significantly enhance the atomic flux within CCAs, which is more conducive to dislocation movement and grain boundary migration. In addition, the electronic wind force caused by the instantaneous input of a large number of high-speed moving electrons during the EPT process can also accelerate dislocation movement and promote grain boundary migration. Thanks to the instantaneous input of a large number of high-energy electrons, the unique electroplastic effect of high-energy pulse current treatment can cause recrystallization of high entropy alloys in a short period of time. As shown in Fig. 6a and b, most of the original columnar grains have been replaced by coarsened equiaxed grains. Fig. 6g and h indicate that the recovery grain area fractions of the SLM-$Al_{0.5}$CoCrFeNi CCA and 90V/30s states are 33.9 % and 79.6 %, and the recrystallization grain area fractions are 3.6 % and 17.9 %, respectively. These results indicate that EPT promotes rapid recrystallization in a shorter period of time. In addition, the EPT time is extremely short, and some recrystallized grains do not have enough growth time.

Some studies have reported the mechanism of the effect of EPT on recrystallization, mainly because the pulse current reduces the nucleation potential barrier of recrystallization [33,62]. The variation of nucleation barrier ΔG_e can be represented by the following formula:

$$\Delta G_e = \mu \bullet g \frac{(\sigma_2 - \sigma_1)}{(\sigma_2 + 2\sigma_1)} \bullet j^2 \bullet V \tag{3}$$

μ is the magnetic susceptibility, g is a positive geometric factor that depends on the parent phase and the new phase nucleus. j is the current density, V is the volume of a nucleus. σ_1 and σ_2 are electric conductivities of the parent phase and the new phase. Among them, μ, g, j and V are all constants greater than zero. The nucleation of the new phase reduces defects such as vacancies, resulting in a decrease in conductivity. With $\sigma_1 > \sigma_2$, and it results in $\Delta G_e < 0$. It can be seen that EPT reduces the nucleation barrier of recrystallization, thereby accelerating the recrystallization nucleation of SLM-$Al_{0.5}$CoCrFeNi. Moreover, EPT can achieve recrystallization at lower temperatures. Under the action of pulse current, the 90V30s sample was heated to 713.1 °C to obtain a recrystallized structure similar to traditional heat treatment heating up to 1400 °C [57]. This has also been reported in relevant studies on other materials [34].

From the above analysis, EPT can also promote the transition from FCC phase to BCC phase by decreasing thermodynamic barriers. As reported in the previous study, $\sigma_{FCC} > \sigma_{BCC}$, and it results in $\Delta G_{FCC \rightarrow BCC} < 0$ [63]. At the 90V/30s EPT state, BCC phase precipitates from grain boundary position within 30 s (Fig. 6c and d).

In conclusion, EPT not only affects atomic diffusion flux through thermal effects, but also plays an important role through non thermal effects. Compared with conventional heat treatment, the non thermal effect in the EPT process can cause some atoms with higher energy deviating from the equilibrium position to migrate towards lower energy equilibrium positions. Under the coupling effect with thermal effect, it can promote the occurrence of recrystallization and phase transition in a short period of time.

5. Conclusions

In this study, the effect of EPT on the SLM-$Al_{0.5}$CoCrFeNi CCA was analyzed. The microstructure of samples with different EPT states were characterized. The strengthening and softening mechanism were revealed. The following conclusions can be drawn from this study:

(1) Dislocation network is a key factor that affects the strength and microhardness of SLM-$Al_{0.5}$CoCrFeNi CCA.
(2) Electronic wind force can effectively alter the dislocation structure in SLM-$Al_{0.5}$CoCrFeNi CCA, thereby affecting its strength and microhardness.
(3) EPT promotes recrystallization and the transition from FCC phase to BCC phase in a short time by lowering the thermodynamic barrier.
(4) EPT can control microstructure and mechanical properties by adjusting parameters, and has broad application prospects in the field of additive manufacturing CCAs post-processing.

CRediT authorship contribution statement

Bo Jiao: Writing – original draft, Formal analysis. **Yuhui Du:** Methodology, Investigation, Conceptualization. **Chunhuan Guo:** Writing – review & editing, Project administration. **Fengchun Jiang:** Supervision, Resources. **Qianfei Sun:** Investigation. **Hexin Zhang:** Investigation. **Tao Dong:** Visualization. **Zubin Chen:** Investigation. **Sergey Konovalov:** Visualization.

Declaration of competing interest

The authors declare the following financial interests/personal relationships which may be considered as potential competing interests:

I write on behalf of myself and all co-authors to confirm that the results reported in the manuscript are original and neither the entire work, nor any of its parts have been previously published. The authors confirm that the article has not been submitted to peer review, nor has been accepted for publishing in another journal. The author(s) confirms that the research in their work is original, and that all the data given in the article are real and authentic. If necessary, the article can be recalled, and errors corrected.

Data availability

Data will be made available on request.

Acknowledgments

This work was supported by the National Key R&D Program of China (No. 2021YFC2801904), the Science Fund of Shandong Laboratory of Advanced Materials and Green Manufacturing (Yantai) (No. AMGM2021F01), and Fundamental Research funds for the Central Universities (3072021CFT1012).

Appendix A. Supplementary data

Supplementary data to this article can be found online at https://doi.org/10.1016/j.msea.2023.146017.

References

[1] J.W. Yeh, S.K. Chen, S.J. Lin, J.Y. Gan, T.S. Chin, T.T. Shun, C.H. Tsau, S.Y. Chang, Nanostructured high-entropy alloys with multiple principal elements: novel alloy design concepts and outcomes, Adv. Eng. Mater. 6 (5) (2004) 299–303.
[2] B. Cantor, I.T.H. Chang, P. Knight, A.J.B. Vincent, Microstructural development in equiatomic multicomponent alloys, Mater. Sci. Eng., A 375–377 (2004) 213–218.
[3] C. Zhang, C. Zhu, K. Vecchio, Non-equiatomic FeNiCoAl-based high entropy alloys with multiscale heterogeneous lamella structure for strength and ductility, Mater. Sci. Eng., A 743 (2019) 361–371.
[4] P.F. Zhou, D.H. Xiao, Z. Wu, X.Q. Ou, Al0.5FeCoCrNi high entropy alloy prepared by selective laser melting with gas-atomized pre-alloy powders, Materials Science and Engineering a-Structural Materials Properties Microstructure and Processing 739 (2019) 86–89.
[5] G.N. Ji, J. Xiang, R.D. Zhao, F.F. Wu, S.H. Chen, Microstructure and mechanical properties of NixFeCoCrAl high-entropy alloys, Mater. Today Commun. 32 (2022), 103919.
[6] A. Amar, M. Wang, L. Zhang, J. Li, L. Huang, H. Yan, Y. Zhang, Y. Lu, Additive manufacturing of VCoNi medium-entropy alloy: microstructure evolution and mechanical properties, Addit. Manuf. 68 (2023), 103522.
[7] Y. Zhang, T.T. Zuo, Z. Tang, M.C. Gao, K.A. Dahmen, P.K. Liaw, Z.P. Lu, Microstructures and properties of high-entropy alloys, Prog. Mater. Sci. 61 (2014) 1–93.
[8] M. Ogura, T. Fukushima, R. Zeller, P.H. Dederichs, Structure of the high-entropy alloy AlxCrFeCoNi: fcc versus bcc, J. Alloys Compd. 715 (2017) 454–459.
[9] J.K. Jensen, B.A. Welk, R.E.A. Williams, J.M. Sosa, D.E. Huber, O.N. Senkov, G. B. Viswanathan, H.L. Fraser, Characterization of the microstructure of the compositionally complex alloy $Al_1Mo_{0.5}Nb_1Ta_{0.5}Ti_1Zr_1$, Scripta Mater. 121 (2016) 1–4.
[10] S. Wolff-Goodrich, O. Shuleshova, I. Kaban, C.H. Liebscher, Revealing complex microstructure formation mechanisms in the $Al_{20}Cr_{20}Fe_{35}Ni_{20}Ti_5$ compositionally complex alloy, Acta Mater. 229 (2022), 117739.
[11] J. Yeh, S. Lin, Breakthrough applications of high-entropy materials, J. Mater. Res. 33 (19) (2018) 3129–3137.
[12] O. Maulik, D. Kumar, S. Kumar, S.K. Dewangan, V. Kumar, Structure and properties of lightweight high entropy alloys: a brief review, Mater. Res. Express 5 (5) (2018), 052001.
[13] Z.Y. Ye, J.N. Li, L.Q. Liu, F.K. Ma, B. Zhao, X.L. Wang, Microstructure and wear performance enhancement of carbon nanotubes reinforced composite coatings fabricated by laser cladding on titanium alloy, Opt Laser. Technol. 139 (2021), 106957.
[14] H. Liu, X.J. Li, J. Liu, W.P. Gao, X.T. Du, J.B. Hao, Microstructural evolution and properties of dual-layer $CoCrFeMnTi_{0.2}$ high-entropy alloy coating fabricated by laser cladding, Opt Laser. Technol. 134 (2021), 106646.
[15] S.Y. Wu, D.X. Qiao, H.L. Zhao, J. Wang, Y.P. Lu, A novel $NbTaW_{0.5}$ $(Mo_2C)_x$ refractory high-entropy alloy with excellent mechanical properties, J. Alloys Compd. 889 (2021), 161800.
[16] Y.C. Yang, Y.J. Ren, Y.W. Tian, K.Y. Li, W.D. Zhang, Q. Shan, Y.T. Tian, Q. L. Huang, H. Wu, Microstructure and properties of FeCoCrNiMoSix high-entropy alloys fabricated by spark plasma sintering, J. Alloys Compd. 884 (2021), 161070.
[17] C.J. Han, Q.H. Fang, Y.S. Shi, S.B. Tor, C.K. Chua, K. Zhou, Recent advances on high-entropy alloys for 3D printing, Adv. Mater. 32 (26) (2020), 1903855.
[18] A.O. Moghaddam, N.A. Shaburova, M.N. Samodurova, A. Abdollahzadeh, E. A. Trofimov, Additive manufacturing of high entropy alloys: a practical review, J. Mater. Sci. Technol. 77 (2021) 131–162.
[19] P. Wang, J.F. Qi, Z.W. Chen, C.S. Lao, T.B. He, T.W. Lu, P. Gargarella, S. Scudino, Microstructure and mechanical properties of novel high-entropy alloy particle reinforced aluminum matrix composites fabricated by selective laser melting, J. Alloys Compd. 868 (2021), 159197.

[20] Z.G. Zhu, Q.B. Nguyen, F.L. Ng, X.H. An, X.Z. Liao, P.K. Liaw, S.M.L. Nai, J. Wei, Hierarchical microstructure and strengthening mechanisms of a CoCrFeNiMn high entropy alloy additively manufactured by selective laser melting, Scripta Mater. 154 (2018) 20–24.
[21] Y. Mu, L. He, S. Deng, Y. Jia, Y. Jia, G. Wang, Q. Zhai, P.K. Liaw, C.-T. Liu, A high-entropy alloy with dislocation-precipitate skeleton for ultrastrength and ductility, Acta Mater. 232 (2022), 117975.
[22] T. Kimura, T. Nakamoto, Microstructures and mechanical properties of A356 (AlSi7Mg0.3) aluminum alloy fabricated by selective laser melting, Mater. Des. 89 (2016) 1294–1301.
[23] D.Y. Lin, L.Y. Xu, H.Y. Jing, Y.D. Han, L. Zhao, F. Minami, Effects of annealing on the structure and mechanical properties of FeCoCrNi high-entropy alloy fabricated via selective laser melting, Addit. Manuf. 32 (2020), 101058.
[24] R. Li, P. Niu, T. Yuan, P. Cao, C. Chen, K. Zhou, Selective laser melting of an equiatomic CoCrFeMnNi high-entropy alloy: processability, non-equilibrium microstructure and mechanical property, J. Alloys Compd. 746 (2018) 125–134.
[25] D. Yuan, S.Q. Shao, C.H. Guo, F.C. Jiang, J.D. Wang, Grain refining of Ti-6Al-4V alloy fabricated by laser and wire additive manufacturing assisted with ultrasonic vibration, Ultrason. Sonochem. 73 (2021), 105472.
[26] D. Yuan, X.J. Sun, L.B. Sun, Z.C. Zhang, C.H. Guo, J.D. Wang, F.C. Jiang, Improvement of the grain structure and mechanical properties of austenitic stainless steel fabricated by laser and wire additive manufacturing assisted with ultrasonic vibration, Materials Science and Engineering a-Structural Materials Properties Microstructure and Processing 813 (2021), 141177.
[27] C.J. Todaro, M.A. Easton, D. Qiu, D. Zhang, M.J. Bermingham, E.W. Lui, M. Brandt, D.H. StJohn, M. Qian, Grain structure control during metal 3D printing by high-intensity ultrasound, Nat. Commun. 11 (1) (2020), 101632.
[28] M.X. Diao, C.H. Guo, Q.F. Sun, F.C. Jiang, L.Y. Li, J.F. Li, D. Xu, C.M. Liu, H. L. Song, Improving mechanical properties of austenitic stainless steel by the grain refinement in wire and arc additive manufacturing assisted with ultrasonic impact treatment, Materials Science and Engineering a-Structural Materials Properties Microstructure and Processing 857 (2022), 144044.
[29] Y. Lu, X. Wu, Z. Fu, Q. Yang, Y. Zhang, Q. Liu, T. Li, Y. Tian, H. Tan, Z. Li, T. Wang, T. Li, Ductile and ultrahigh-strength eutectic high-entropy alloys by large-volume 3D printing, J. Mater. Sci. Technol. 126 (2022) 15–21.
[30] T. Fujieda, H. Shiratori, K. Kuwabara, M. Hirota, T. Kato, K. Yamanaka, Y. Koizumi, A. Chiba, S. Watanabe, CoCrFeNiTi-based high-entropy alloy with superior tensile strength and corrosion resistance achieved by a combination of additive manufacturing using selective electron beam melting and solution treatment, Mater. Lett. 189 (2017) 148–151.
[31] J. Joseph, P. Hodgson, T. Jarvis, X.H. Wu, N. Stanford, D.M. Fabijanic, Effect of hot isostatic pressing on the microstructure and mechanical properties of additive manufactured AlxCoCrFeNi high entropy alloys, Mater. Sci. Eng. A-Struct. Mater. Prop. Microstruct. Process. 733 (2018) 59–70.
[32] Z.Q. Cui, Y.J. Mi, D. Qiu, P. Dong, Z. Qin, D.Q. Gong, W.G. Li, Microstructure and mechanical properties of additively manufactured CrMnFeCoNi high-entropy alloys after ultrasonic surface rolling process, J. Alloys Compd. 887 (2021), 161393.
[33] J.B. Gao, D.D. Ben, H.J. Yang, L.X. Meng, H.B. Ji, D.L. Lian, J. Chen, J.L. Yi, L. Wang, P. Li, Z.F. Zhang, Effects of electropulsing on the microstructure and microhardness of a selective laser melted Ti6Al4V alloy, J. Alloys Compd. 875 (2021), 160044.
[34] R. Zhu, Y. Jiang, L. Guan, H. Li, G. Tang, Difference in recrystallization between electropulsing-treated and furnace-treated NiTi alloy, J. Alloys Compd. 658 (2016) 548–554.
[35] X.F. Xu, X.D. Yan, Y. Qian, X.Y. Chong, Y.C. Zhou, Y.G. Zhao, X.H. Yang, G.F. Liu, C. Wu, Ti-6Al-4V alloy strengthening via instantaneous phase transformation induced by electropulsing, J. Alloys Compd. 899 (2022), 163303.
[36] D. Waryoba, Z. Islam, T. Reutzel, A. Haque, Electro-strengthening of the additively manufactured Ti-6Al-4V alloy, Materials Science and Engineering a-Structural Materials Properties Microstructure and Processing 798 (2020), 140062.
[37] Z. Islam, H. Gao, A. Haque, Synergy of elastic strain energy and electron wind force on thin film grain growth at room temperature, Mater. Char. 152 (2019) 85–93.
[38] D. Waryoba, Z. Islam, B. Wang, A. Haque, Low temperature annealing of metals with electrical wind force effects, J. Mater. Sci. Technol. 35 (4) (2019) 465–472.
[39] S.Q. Xiang, X.F. Zhang, Dislocation structure evolution under electroplastic effect, Materials Science and Engineering a-Structural Materials Properties Microstructure and Processing 761 (2019), 138026.
[40] Y. Yuan, W. Liu, B. Fu, H. Xu, G. Luo, G. Tang, Y. Jiang, The effects of electropulsing on the recrystallization behavior of rolled pure tungsten, J. Mater. Res. 27 (20) (2012) 2630–2638.
[41] X. Zhang, H. Li, M. Zhan, Z. Zheng, J. Gao, G. Shao, Electron force-induced dislocations annihilation and regeneration of a superalloy through electrical in-situ transmission electron microscopy observations, J. Mater. Sci. Technol. 36 (2020) 79–83.
[42] K.M. Klimov, G.D. Shnyrev, I.I. Novikov, Electroplasticity " of metals, Sov. Phys. Dokl. 19 (1975) 787.
[43] L. Guan, G. Tang, P.K. Chu, Recent advances and challenges in electroplastic manufacturing processing of metals, J. Mater. Res. 25 (7) (2010) 1215–1224.
[44] C.L. Liang, K.L. Lin, The microstructure and property variations of metals induced by electric current treatment: a review, Mater. Char. 145 (2018) 545–555.
[45] O.A. Troitskii, V.I. Likhtman, The anisotropy of the action of electron and gamma radiation on the deformation of zinc single crystals in the brittle state, Sov. Phys. Dokl. 8 (1963) 91.
[46] Y.D. Ye, X.P. Li, Z.Y. Sun, H.B. Wang, G.Y. Tang, Enhanced surface mechanical properties and microstructure evolution of commercial pure titanium under electropulsing-assisted ultrasonic surface rolling process, Acta Metallurgica Sinica-English Letters 31 (12) (2018) 1272–1280.
[47] X.P. Li, S.Z. Kure Chu, T. Ogasawara, H. Yashiro, H.B. Wang, Z.Z. Xu, X.H. Li, G. L. Song, G.Y. Tang, Fabrication of a gradient nano-/micro-structured surface layer on an Al-Si casting alloy by means of ultrasonic-electropulsing coupling rolling process, Acta Metallurgica Sinica-English Letters 31 (12) (2018) 1258–1264.
[48] M. Aizenshtein, E. Strumza, E. Brosh, S. Hayun, Microstructure, kinetics and thermodynamics of HEA $Al_{0.5}$CoCrFeNi at T $\geq$ 800 °C, Mater. Char. 171 (2021), 110738.
[49] C.M. Lin, H.L. Tsai, Evolution of microstructure, hardness, and corrosion properties of high-entropy $Al_{0.5}$CoCrFeNi alloy, Intermetallics 19 (3) (2011) 288–294.
[50] L. Liu, Q. Ding, Y. Zhong, J. Zou, J. Wu, Y.-L. Chiu, J. Li, Z. Zhang, Q. Yu, Z. Shen, Dislocation network in additive manufactured steel breaks strength-ductility trade-off, Mater. Today 21 (4) (2018) 354–361.
[51] K. Sun, W.X. Peng, L.L. Yang, L. Fang, Effect of SLM processing parameters on microstructures and mechanical properties of Al0.5CoCrFeNi high entropy alloys, Metals 10 (2) (2020) 292.
[52] K. Xiong, L. Huang, X.F. Wang, L. Yu, W. Feng, Cooling-rate effect on microstructure and mechanical properties of Al0.5CoCrFeNi high-entropy alloy, Metals 12 (8) (2022) 1254.
[53] A. Ghaderi, H. Moghanni, K. Dehghani, Microstructural evolution and mechanical properties of Al0.5CoCrFeNi high-entropy alloy after cold rolling and annealing treatments, J. Mater. Eng. Perform. 30 (10) (2021) 7817–7825.
[54] J. Wang, H.X. Yang, T. Guo, J.X. Wang, W.Y. Wang, J.S. Li, Effect of cold rolling on the phase transformation kinetics of an Al0.5CoCrFeNi high-entropy alloy, Entropy 20 (12) (2018) 917.
[55] H.C. Li, J. Wang, H.X. Yang, M.M. Zhao, W.Y. Wang, R.H. Yuan, J.S. Li, Nanoscale B2 precipitation and strengthening behavior in Al0.5CoCrFeNi high-entropy alloy, Mater. Char. 191 (2022), 112156.
[56] J. Wang, S. Niu, T. Guo, H. Kou, J. Li, The FCC to BCC phase transformation kinetics in an Al0.5CoCrFeNi high entropy alloy, J. Alloys Compd. 710 (2017) 144–150.
[57] Y.H. Du, C.H. Guo, F.C. Jiang, Y.C. Li, X.J. Sun, Q.F. Sun, H.X. Zhang, T. Dong, S. Konovalov, Effect of heat treatment on microstructure and properties of Al0.5CoCrFeNi high entropy alloy fabricated by selective laser melting, Materials Science and Engineering a-Structural Materials Properties Microstructure and Processing 882 (2023), 145466.
[58] M.B. Kivy, M.A. Zaeem, Generalized stacking fault energies, ductilities, and twinnabilities of CoCrFeNi-based face-centered cubic high entropy alloys, Scripta Mater. 139 (2017) 83–86.
[59] C.H. Lee, Y. Chou, G. Kim, M.C. Gao, K. An, J. Brechtl, C. Zhang, W. Chen, J. D. Poplawsky, G. Song, Y. Ren, Y.C. Chou, P.K. Liaw, Lattice-distortion-enhanced yield strength in a refractory high-entropy alloy, Adv. Mater. 32 (49) (2020), 2004029.
[60] Y.H. Zhu, S. To, W.B. Lee, X.M. Liu, Y.B. Jiang, G.Y. Tang, Effects of dynamic electropulsing on microstructure and elongation of a Zn-Al alloy, Materials Science and Engineering a-Structural Materials Properties Microstructure and Processing 501 (1–2) (2009) 125–132.
[61] X.N. Du, S.M. Yin, S.C. Liu, B.Q. Wang, J.D. Guo, Effect of the electropulsing on mechanical properties and microstructure of an ECAPed AZ31 Mg alloy, J. Mater. Res. 23 (6) (2008) 1570–1577.
[62] Y.Z. Zhou, W. Zhang, B.Q. Wang, G.H. He, J.D. Guo, Grain refinement and formation of ultrafine-grained microstructure in a low-carbon steel under electropulsing, J. Mater. Res. 17 (8) (2002) 2105–2111.
[63] H.P. Chou, Y.S. Chang, S.K. Chen, J.W. Yeh, Microstructure, thermophysical and electrical properties in Al_xCoCrFeNi ($0 \leq x \leq 2$) high-entropy alloys, Materials Science and Engineering B-Advanced Functional Solid-State Materials 163 (3) (2009) 184–189.